

## MICROSTRUCTURE AND EROSION WEAR CHARACTERIZATION OF A NEW CAST HIGH-VANADIUM–CHROMIUM ALLOY (HVCA)

Fangfang Wang  and Liujie Xu

School of Materials Science and Engineering, Henan University of Science and Technology, Luoyang 471003, China  
National Joint Engineering Research Center for Abrasion Control and Molding of Metal Materials, Henan University of Science and Technology, Luoyang 471003, China

Copyright © 2022 American Foundry Society  
<https://doi.org/10.1007/s40962-022-00787-9>

### Abstract

To evaluate the enhanced erosion wear performance under acidic medium, a new high-vanadium–chromium alloy (HVCA) is designed and test samples produced by sand casting. The microstructure was analyzed by SEM, TEM and XRD. The erosion wear performance was tested in acidic medium designed by orthogonal test method. The factors affecting the erosion wear performance of HVCA are analyzed. The research results show that microstructure of HVCA is characterized by different carbides ( $M_7C_3$ ,  $M_{23}C_6$ , VC,  $M_2C$ ) distributed in martensite and residual austenite. The hardness is  $65.16 \pm 0.2$  HRC, and the impact toughness is  $9.82 \pm 0.12$  J/cm<sup>2</sup>.  $H_2SO_4$

concentration has the greatest influence on the erosion wear performance of HVCA, followed by the erosion wear angle. The maximum erosion wear performance of HVCA is 1.59 times that of HCCI. Compared with HCCI, HVCA has excellent erosion wear resistance because of its high hardness and toughness, a small amount of fracture and carbide shedding, and slight corrosion and wear interaction under erosion wear condition.

**Keywords:** high-vanadium–chromium alloy, carbide, erosion wear, orthogonal test

### Introduction

Slag slurry pump is an industrial pump for transporting slurry with solid particles in electric power, mining, chemical industry and environmental protection industry.<sup>1–4</sup> The special failure mode of slurry pump is corrosion wear, which is the result of the interaction of chemical and mechanical factors. Erosion wear is caused by high-speed relative movement between slurry and material surface, and it is the interaction of corrosion and wear. The corrosion wear action of erosion wear is very different from the single erosion or wear, which can accelerate the material damage.<sup>5–7</sup> Erosion wear has become an inevitable factor to destroy facilities or materials.<sup>8</sup> There are many factors affecting erosion wear, mainly including the type and concentration of slurry corrosion medium, the size and shape of solid particles, and the selection of materials, etc.<sup>9–11</sup>

High-chromium cast irons (HCCIs) are excellent wear-resistant materials.<sup>12,13</sup> At present, the slurry pumps is usually made of high-chromium cast irons, which have good erosion wear properties in non-corrosive water sand slurry. However, the chromium carbides, such as  $Cr_7C_3$ ,  $Cr_{23}C_6$  and  $Cr_2C$ , have relatively low hardness compared with other MC-type carbides such as VC, TiC and WC. To get high-hardness carbides in alloy is an important way to improve wear resistance of materials.<sup>12,14–16</sup> According to previous studies, vanadium carbide in alloys could improve wear resistance of materials significantly.<sup>17–19</sup> Besides, adding vanadium element into HCCI can refine grain, improve microstructure and increase secondary carbide content.<sup>20,21</sup> Secondly, carbide precipitation plays an important role in improving the wear performance of HCCI, because it ensures the high hardness of the matrix region and promotes the precipitation. Meanwhile, the corrosion resistance can be improved to some extent.<sup>22,23</sup> However, there are few studies on erosion resistance of high-vanadium–chromium alloy (HVCA).

In this paper, a large amount of vanadium element was added to HCCI to obtain a new wear-resistant alloy called HVCA. The factors affecting the erosion wear of the new HVCA are analyzed by orthogonal test and variance analysis. At the same time, the erosion wear behavior and mechanism of HVCA in water mortar and acid mortar are studied, and the interaction of erosion wear was analyzed. In HCCI, the same experiment was conducted as a comparative material.

## Experimental Methods

### Materials

Test samples of both HVCA and HCCI melted in a medium-frequency induction furnace were cast by using an ordinary sand casting method. The raw materials with a good ratio of pig iron, high-carbon chromium, molybdenum manganese and nitrogen are put into the furnace melting, melting after adding aluminum blocks for deoxidation treatment and then adding vanadium ferroalloy. When the temperature of molten iron is between 1500 and 1550 °C, the samples are sampled and tested. After adjusting the composition to meet the requirements, the molten iron is poured into the steel ingot mold with rare earth modifier to cool and form, and the alloy ingot with high-vanadium wear resistance and erosion resistance is obtained. The size is about 30 mm × 5 mm × 250 mm. The actual chemical composition of the samples is shown in Table 1.

The heat treatment process of this experiment is 1050 °C quenching and 250 °C low-temperature tempering (as shown in Figure 1), which is carried out in the BSK-83 resistance furnace. The furnace has automatic temperature control and heat preservation function. At the beginning of quenching, the heating speed is relatively low (50 °C/h), because HCCI is heated too fast and easy to crack, so it should be heated to 800 °C for 1 h, and then accelerated (100 °C/h). Due to the high content of carbon and alloying elements in the material, too low quenching temperature will make a lot of carbide not to be dissolved into austenitic during the austenitizing process. Therefore, the wear resistance and impact toughness can be significantly improved by heating to 1050 °C and cooling to room temperature in the air after holding for 1 h.<sup>24</sup> In the tempering process, it is heated to 250 °C at the speed of

100 °C/h and cooled to room temperature in the air after holding for 2 h.

### Mechanical Performance Test

The microhardness of matrix and carbide was measured by digital microhardness tester (HVT-1000). The test load was 50 g, and the average value of 10 points was taken as the hardness value. HR-150A Rockwell hardness tester was used to test the hardness of the sample. The test surface of the sample was required to be smooth. In the process of measurement, measure the average hardness of five experimental points with a distance of more than 3 mm. The impact toughness of the sample was measured by JB-300B (pendulum) impact testing machine. The sample is a defect-free standard sample with a size of 20 mm × 20 mm × 110 mm. Span is 70 mm.

### Erosion-Wear Performance Test

Erosion wear test was carried out with L9 orthogonal matrix. Table 2 lists the test parameters varying according to the design matrix. The MM-20CF (as shown in Figure 2) rotary erosion and wear testing machine is used to test the erosion and wear properties of materials. The sample is installed on the edge of the test tank, and the erosion angle is adjusted by changing the sample clamp. The material of the turntable and sample clamp is PTFC. The clamping method of the sample is as shown in Figure 3. The top of the sample is clamped with a plastic gasket made of the same material as the sample clamp. The shape and size of the sample are shown in Figure 4. The side of the sample is the erosion wear test surface of 12 mm × 30 mm.

The slurry type includes water mortar and acid mortar. The total mass of mortar in the corrosion tank is 40 kg, the mass fraction of quartz sand is 40%, and the erosion time is 4 h. The water in the slurry is city tap water. The particle size of quartz sand in slurry was analyzed by LS-909 laser particle size analyzer. The particle size range of quartz sand is 232–1600 μm, and its hardness is 1120 HV. Silicon sand particles have sharp edges and bad roundness. The particle size distribution of sand is shown in Figure 5. The average particle size of sand particles is 773.1 μm, and the average spherical size is 0.58. The effects of erosion velocity (500 r/min, 750 r/min, 1000 r/min), erosion angle

**Table 1. Chemical Composition of Materials (wt%)**

Materials	C	Cr	V	Si	Mn	Mo	P, S
Target	3–3.2	14.5–15.5	5.5–6.5	0.5–1	0.5–1	3.5–4.5	≤ 0.07
HVCA	3.08	15.03	6.511	0.91	0.91	4.3	≤ 0.07
HCCI	3.06	23.01	–	0.62	1.15	0.507	≤ 0.07

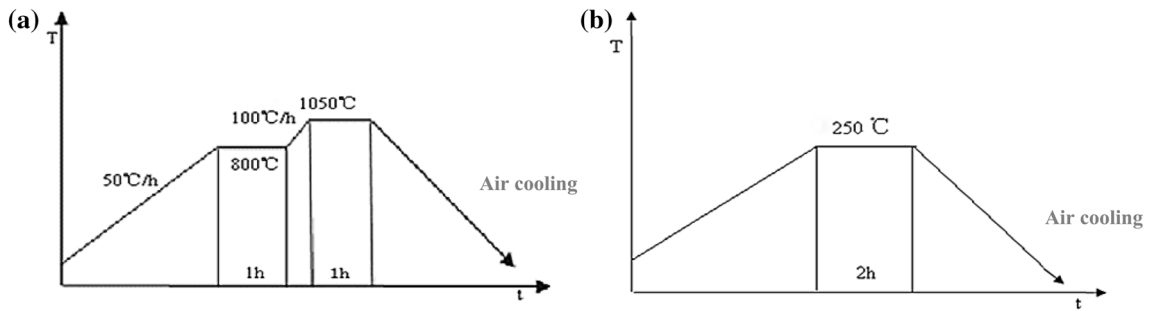


Figure 1. Heat treatment process: (a) quenching, (b) tempering.

Table 2. Testing Parameters for Erosion Experiments

Factors	Level 1	Level 2	Level 3
Velocity (r/min)	500	750	1000
Angle of impingement (°)	30	45	60
H <sub>2</sub> SO <sub>4</sub> concentration (wt%)	2	4	6

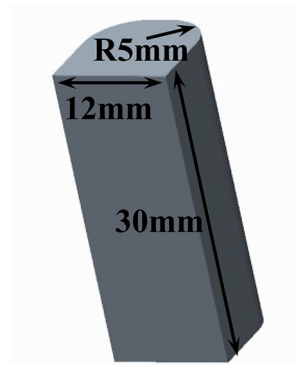


Figure 4. The shape and size of the specimen.

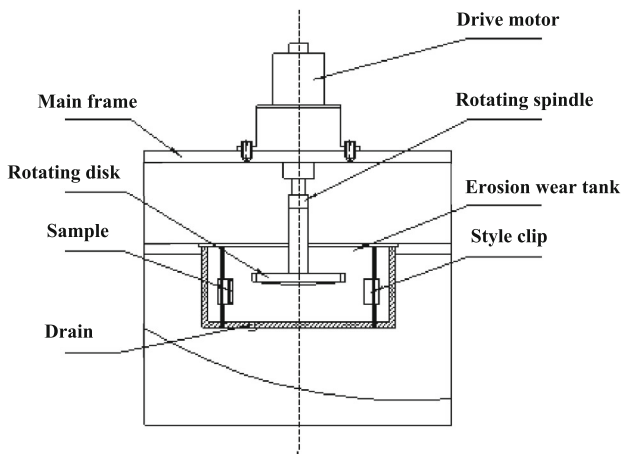


Figure 2. The schematic diagram of MM-20CF erosion wear testing machine.

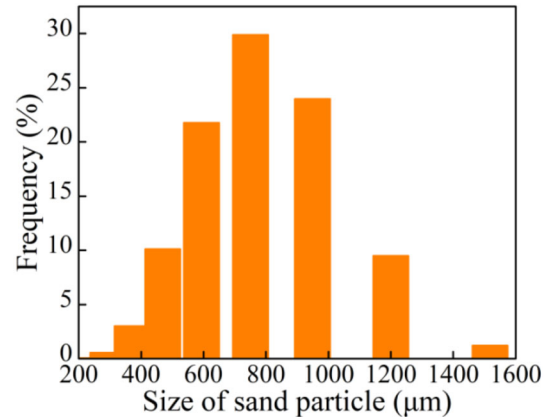


Figure 5. Size distribution of the silica sand particles.

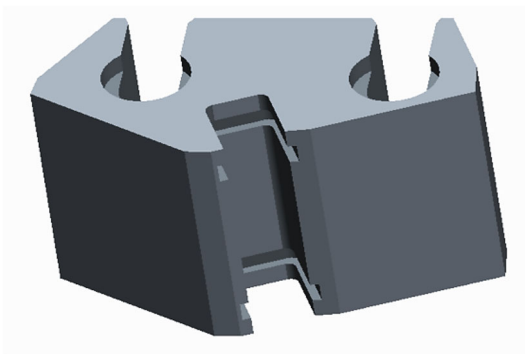


Figure 3. Clamping method of the specimen.

(30°, 45°, 60°) and acid concentration (2 wt%, 4 wt%, 6 wt%) on erosion wear were studied at room temperature. In order to ensure the validity of the test data, three parallel tests should be conducted for each group.

The main parameters to study the erosion wear performance of the material are erosion wear rate  $V_b$ , interaction rate of corrosion and wear  $V_s$ , pure wear rate  $V_e$ , pure corrosion rate  $V_c$ , and the relative erosion wear resistance  $\varepsilon$  of the high-vanadium alloy. The expressed of  $V_t$  is as follows:

$$V_t = V_s + V_c + V_e \quad \text{Eqn. 1}$$

In the formula,  $V_t$  can directly take the loss amount of the material after erosion and wear in the acid mortar,  $V_e$  can directly take the loss amount of the material after erosion and wear in water mortar, and  $V_c$  is obtained by the loss amount after static corrosion. The units are converted into  $\text{g m}^{-2} \text{h}^{-1}$ .

The relative erosion resistance coefficient ( $\varepsilon$ ) was used to characterize the erosion resistance of the material, and the expression was as follows:

$$\varepsilon = W_s/W_c \quad \text{Eqn. 2}$$

$W_s$  is the mass loss of ordinary high-chromium cast iron after erosion and wear, while  $W_c$  is the mass loss of high-vanadium alloy.

### Microstructural Analysis and Worn Surface Observation

The microstructure was analyzed by scanning electron microscope (VEGA 3-TESCAN-SBH), and the erosion wear morphology was observed. Carbides and matrix elements in the material should be analyzed by EDS, and the phase composition of the material should be determined by XRD (D8 Advanced Bruker, Germany) and transmission electron microscope (Hitachi H—800).

## Results and Discussion

### Microstructure of Materials

Figure 6 shows the XRD diffraction profile of the HVCA after heat treatment, so it can be seen that the microstructure of the HVCA is mainly martensite, residual austenite and carbide ( $M_7C_3$ ,  $M_{23}C_6$ , VC,  $M_2C$ ). The SEM (Figure 7a, b) of the HVCA can be intuitively corresponding, and Figure 6b is a larger version of the  $M_{23}C_6$  region in Figure 7a. The matrix microstructure is refined to a certain

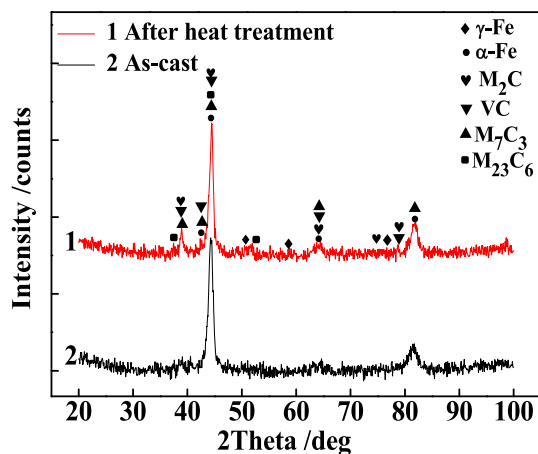


Figure 6. XRD analysis of HVCA.

extent, and the morphology and distribution of carbides are improved to a certain extent. The morphology of carbide changes to granular or blocky, and secondary carbides precipitate. Figure 7c and d shows EDS analysis of area A and area B, respectively, and the small and medium flake carbides in area A are mainly  $M_7C_3$ ,  $M_2C$  and MC. Area B is mainly secondary carbide precipitated from the matrix. The ratio of (Cr, Fe) to C is about 23/6 except for carbides such as  $M_2C$  and VC, indicating that the secondary carbides are  $M_{23}C_6$ -type carbide. The content of eutectic carbide and secondary carbide in high-chromium cast iron, high-vanadium and high-chromium cast iron and high-nitrogen and high-vanadium and high-chromium cast iron after heat treatment was quantitatively calculated by Image Pro Plus software, and the austenite and martensite contents were calculated by XRD (as shown in Table 3). XRD can calibrate the {200} and {211} diffraction peaks of  $\alpha$  phase and {111}, {200} and {311} diffraction peaks of  $\gamma$  phase. The volume fraction of austenite calculated by this method is 15.82%.

Figure 8 shows TEM images and SADP analysis results of secondary carbide  $M_{23}C_6$  with different axes and  $M_{23}C_6$  (PDF 33-0783) with a face-centered cubic structure arranged by atoms in the second phase. The independent and irregular secondary carbide  $M_{23}C_6$  is shown in Figure 7a, with two types of crystal axis:  $[-111]$  and  $[-114]$ .

### Mechanical Properties

Table 4 shows the hardness and impact toughness of the test materials after heat treatment. The hardness and impact toughness of HVCA are 65.16 HRC and  $9.82 \text{ J/cm}^2$ , respectively. The hardness and impact toughness of the HCCI are 56.54 HRC and  $8.45 \text{ J/cm}^2$ , respectively. The hardness and impact toughness of HVCA are better than those of HCCI, so its mechanical properties are better.

### Interaction Plot

Table 5 shows the design matrix of L9 array, in which the observed mass loss is the response to 9 different test conditions. Through the analysis of variance of the effects of all the experimental conditions, the effect intensity of each influence factor was determined statistically. As the smaller the  $P$  value, the greater the effect of the influencing factors, it can be seen that the concentration of  $H_2SO_4$  has the most significant effect on the anti-erosion and wear performance, followed by the erosion and wear angle. It can also be seen from the effect ratio of the influencing factors in Figure 9.

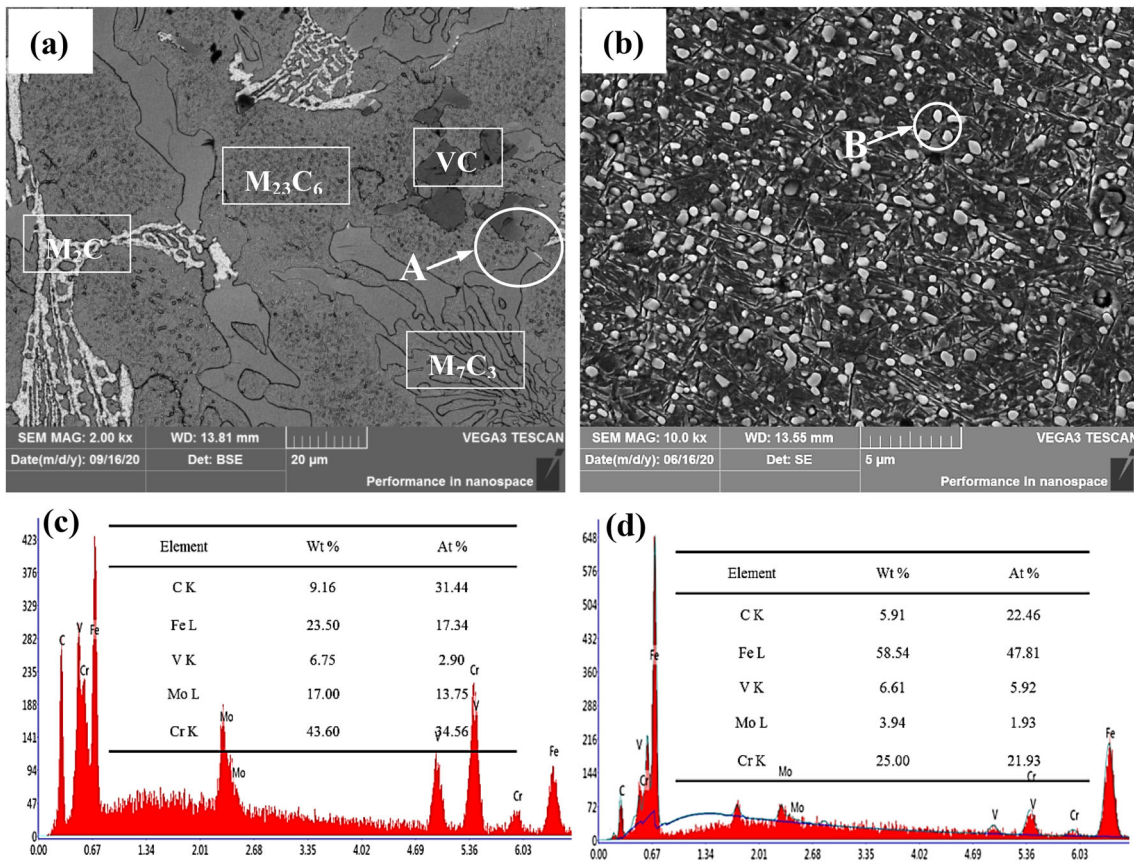


Figure 7. SEM diagram of HVCA: (a) BSE, (b) SE, (c) A area, (d) B area.

Table 3. The Volume Content of Each Phase in the Microstructure After Heat Treatment (vol.%)

Sample	Primary or eutectic carbides	Secondary carbides	Austenite	Martensite
VCr	31	15	15.82	38.18
Cr26	38	8.83	16.36	36.81

Table 4. Mechanical Properties of Materials After Heat Treatment

Materials	Hardness (HRC)	Impact toughness (J/cm <sup>2</sup> )
HVCA	65.16±0.2	9.82±0.12
HCCI	56.54±0.2	8.45±0.12

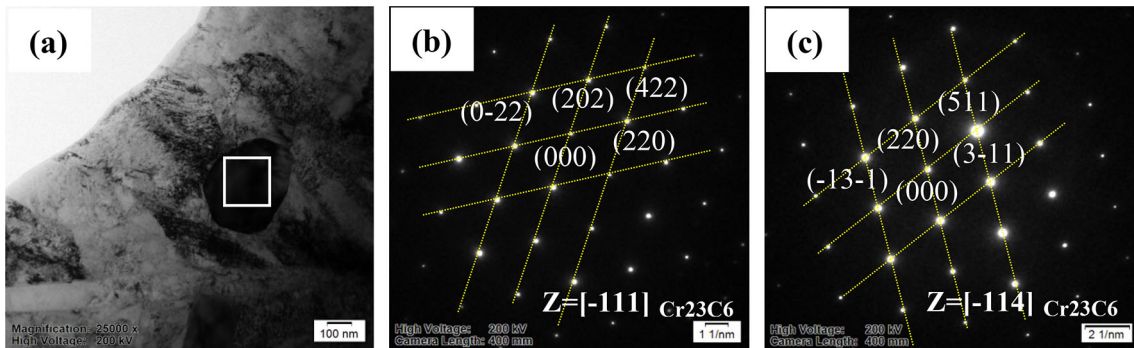
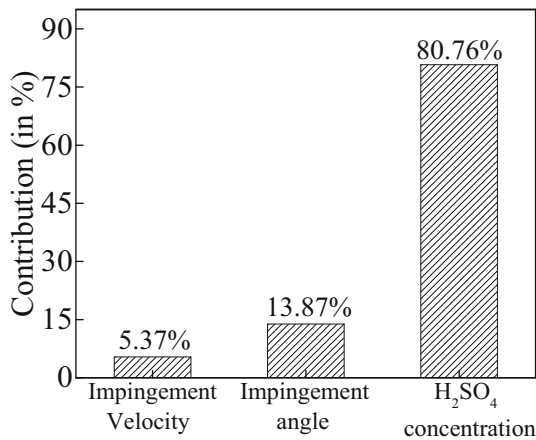


Figure 8. TEM analysis of secondary Cr<sub>23</sub>C<sub>6</sub> carbide: (a) TEM image, (b) and (c) selected area diffraction pattern (SADP) analysis under different zone axes.

**Table 5. Analysis of L9 Orthogonal Array Experimental Data**

Trail no.	Impingement velocity (r/min)	Impingement angle (°)	H <sub>2</sub> SO <sub>4</sub> concentration (wt%)	Mass loss (g)	
1	500	30	2	0.1898	
2	500	45	4	0.4102	
3	500	60	6	0.4275	
4	750	30	4	0.2624	
5	750	45	6	0.3558	
6	750	60	2	0.2863	
7	1000	30	6	0.4022	
8	1000	45	2	0.2360	
9	1000	60	4	0.3285	
$K_1$	0.3425	0.2848	0.2374		
$K_2$	0.3015	0.3340	0.3337		
$K_3$	0.3222	0.3474	0.3952		Error
SS	0.002522	0.006519	0.037957	0.056226	0.009228
df	2	2	2	8	2
MS	0.001261	0.0032595	0.0189785	0.0070283	0.004614
F	0.2732	0.7064	4.1132		
P	0.785423	0.586029	0.195572		



**Figure 9. The contribution of the factors affecting the erosion wear performance.**

### Corrosion Performance

Figure 10 shows the results of static corrosion analysis for these materials. It can be seen from the figure that with the increase in H<sub>2</sub>SO<sub>4</sub> concentration, the corrosion loss weight of the material gradually increases, indicating that the corrosion resistance of the material gradually decreases. Compared with HCCI, HVCA has higher weight loss and lower corrosion resistance.

Figure 11 shows the important characteristics of the electrochemical behaviors of the experimental materials at

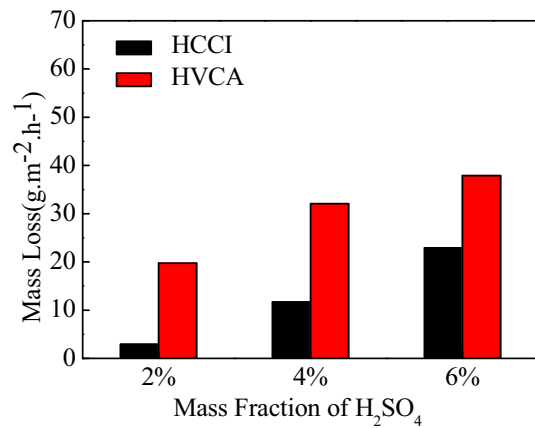


**Figure 10. Static corrosion of materials.**

different concentrations of H<sub>2</sub>SO<sub>4</sub>. Figure 11a and b shows the dynamic potential polarization curves of HVCA and HCCI in H<sub>2</sub>SO<sub>4</sub> solutions with different concentrations. It can be seen from the figure that the dynamic potential polarization curves of each sample are similar. However, in the anode region, HVCA has no obvious passivation interval compared with HCCI. With the increase in H<sub>2</sub>SO<sub>4</sub> concentration, the self-corrosion current density of the material increases gradually and the self-corrosion voltage gradually decreases, indicating that the corrosion resistance of the material becomes worse. The self-corrosive current density of HVCA is always higher than that of HCCI (Figure 11c), and the self-corrosive voltage is always lower

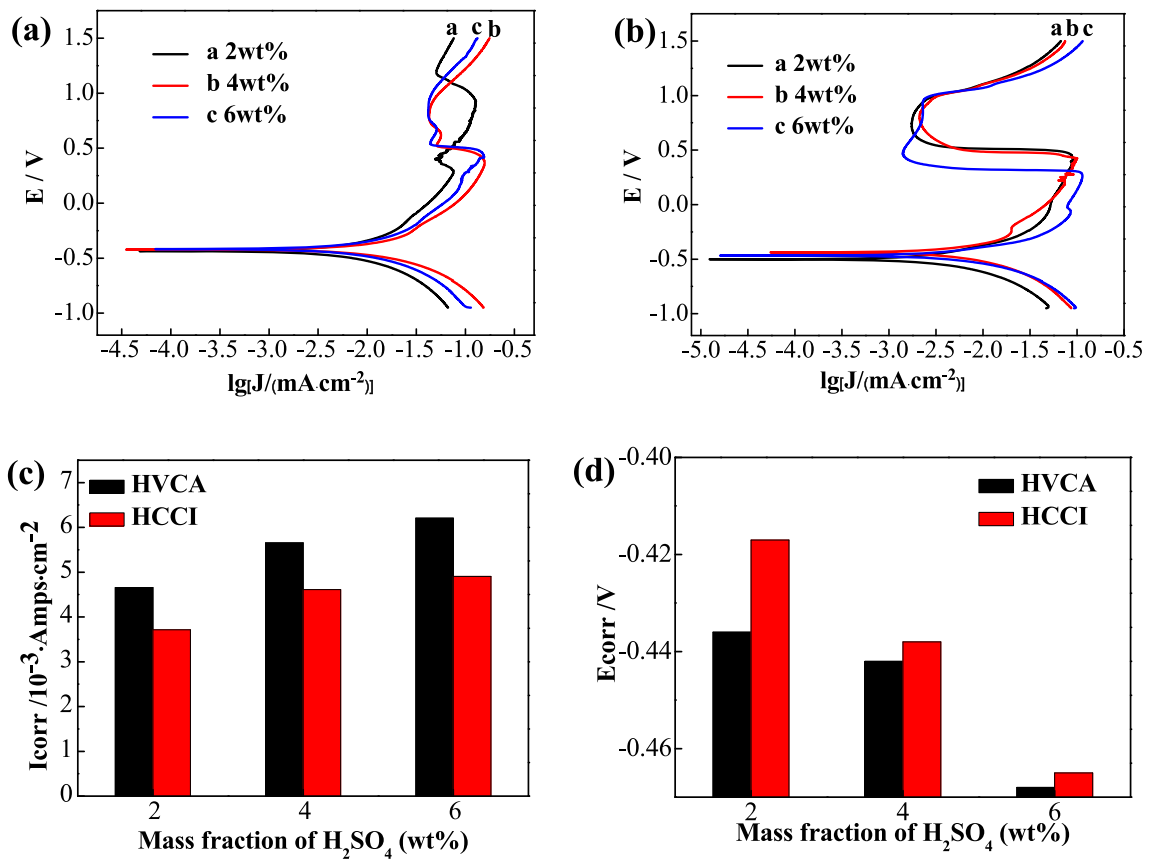


Figure 11. Analysis of material's potentiometric polarization curve: (a) HVCA, (b) HCCI, (c)  $I_{corr}$ , (d)  $E_{corr}$ .

than that of HCCI (Figure 11d), indicating that HVCA has poor corrosion resistance in acid solutions.

### Wear Performance

In water slurry, the erosion wear rate of two materials and relative erosion wear resistance rate ( $\epsilon$ ) of HVCA as shown in Figure 12a. When the erosion wear angle is 45°, the erosion wear rate of the two materials increases with the

increase in erosion wear velocity. When erosion wear velocity between 500 and 1000 r/min, the relative erosion wear resistance rate ( $\epsilon$ ) of HVCA decreases with the increase in erosion wear rate, with the maximum value of 2.05. Figure 12b shows the influence of erosion wear angle on erosion wear rate of the two materials and the relative erosion wear rate ( $\epsilon$ ) of the HVCA. When the erosion wear velocity is 750 r/min, the erosion wear curves of the two materials show similar characteristics. With the increase in erosion wear angle, the erosion wear curves show a trend of

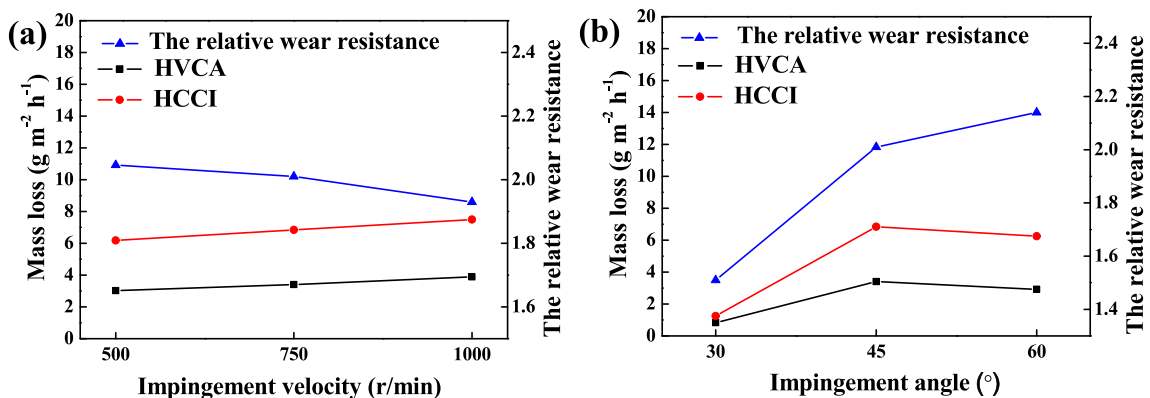


Figure 12. Pure wear rate Vs relative wear resistance ( $\epsilon$ ) of test materials in water mortar: (a) different erosion wear velocities, (b) different erosion wear angles.

increasing at first and then decreasing. When the erosion wear angle is  $60^\circ$ , the erosion wear is the large. The relative erosion resistance wear rate ( $\varepsilon$ ) of HVCA increases with the increase in erosion wear angle, with the maximum value of 2.14.

### Erosion Wear Performance

HVCA mainly composed of eutectic carbides and hard secondary carbide particles, which is brittle and ductile to

some extent. With the increase in impact velocity and impact angle, the erosion wear rate showed a consistent trend. HCCI is also the same. Figure 13a shows the contour diagram of the interaction between erosion velocity and erosion Angle. When the erosion velocity reaches the maximum value or the generation angle is about  $50^\circ$ , HVCA has great erosion wear and poor erosion wear resistance. However, at lower and higher erosion speed and angle, the erosion wear rate of HCCI is larger, because it is mainly affected by corrosion effect at lower condition and mechanical effect at higher condition (Figure 13b).

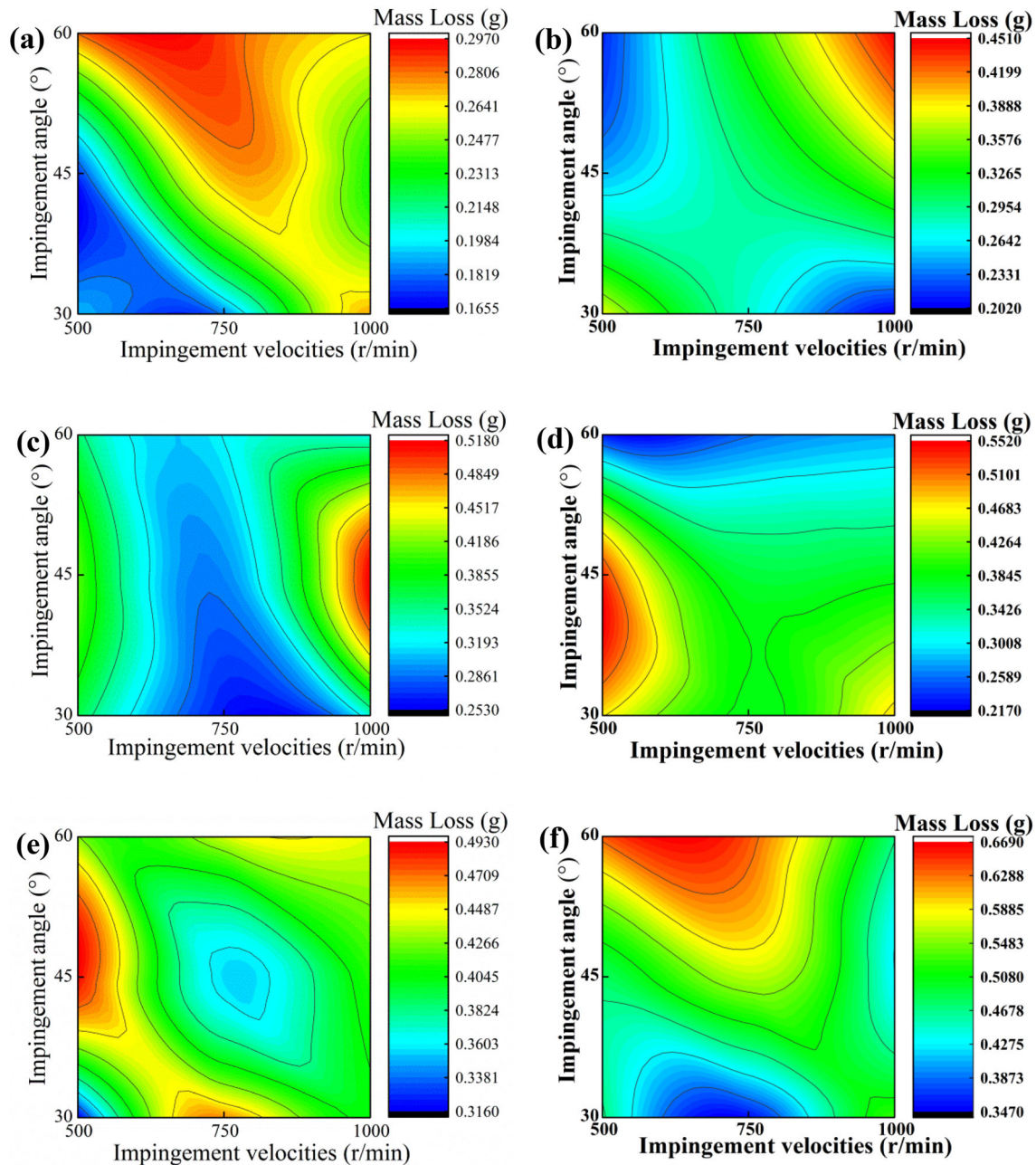


**Figure 13.** The contour plot shows the interactive effect among the influencing factors: (a) HVCA, 2 wt%  $H_2SO_4$ ; (b) HCCI, 2 wt%  $H_2SO_4$ ; (c) HVCA, 4 wt%  $H_2SO_4$ ; (d) HCCI, 4 wt%  $H_2SO_4$ ; (e) HVCA, 6 wt%  $H_2SO_4$ ; (f) HCCI, 6 wt%  $H_2SO_4$ .



Compared with the concentration of  $H_2SO_4$ , the influence of erosion speed can be almost ignored because the concentration of  $H_2SO_4$  and has a significant impact on the erosion wear performance of HVCA, accounting for about 80%. When the concentration of  $H_2SO_4$  is between 4 and 6 wt%, the amount of erosion wear is large and the erosion wear resistance is poor. Erosion angle has a moderate effect on the erosion wear performance of HVCA, which is inferior to the concentration of  $H_2SO_4$ . The influence of erosion angle and  $H_2SO_4$  concentration on erosion wear performance of HVCA is shown in Figure 13c and e. Erosion wear increases with the increase in erosion angle

and  $H_2SO_4$  concentration. When the erosion angle is  $45^\circ$  and the concentration of  $H_2SO_4$  is between 3.5 and 5.5 wt%, the erosion wear is relatively large and the erosion wear performance is poor. With the increase in sulfuric acid concentration, at 4 wt%, the erosion wear rate of HCCI is higher at low erosion wear rate and  $45^\circ$  erosion wear angle. At 6 wt%, the maximum erosion wear rate is at the maximum erosion wear angle and about 750 r/min.

Figure 14 shows the contour map of the interaction between erosion velocity and  $H_2SO_4$  concentration.  $H_2SO_4$  concentration has a significant effect on the erosion wear

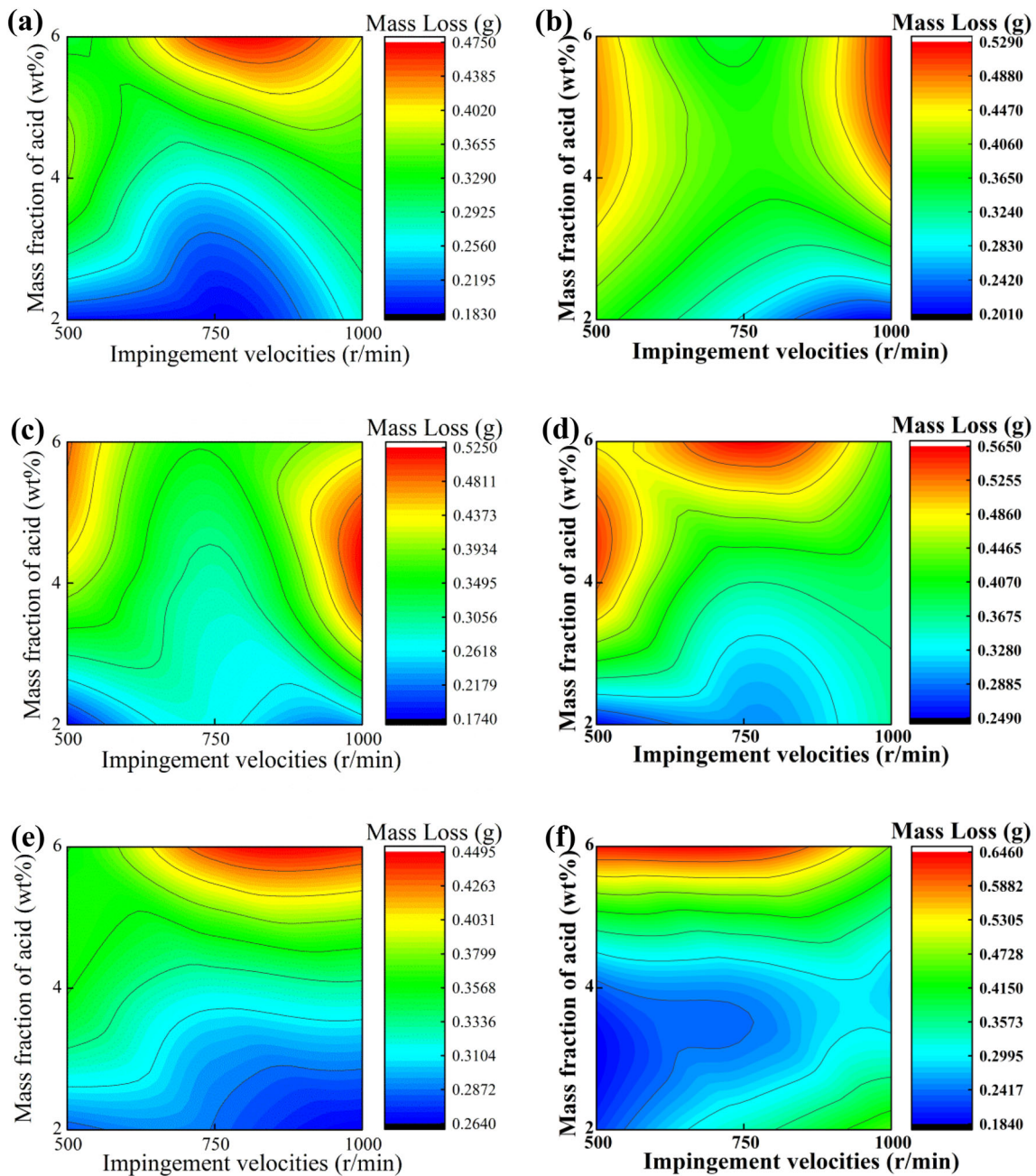


**Figure 14.** The contour plot shows the interactive effect among the influencing factors: (a) HVCA, 30°; (b) HCCI, 30°; (c) HVCA, 45°; (d) HCCI, 45°; (e) HVCA, 60°; (f) HCCI, 60°.

performance of HVCA, accounting for about 80%. Therefore, compared with the effect of  $H_2SO_4$  concentration, the effect of corrosion rate can be almost ignored. As the erosion angle is  $30^\circ$ , the erosion wear of HVCA increases with the increase in  $H_2SO_4$  concentration, and the wear of HCCI is similar to this. However, when the erosion wear rate is low or high and the concentration of  $H_2SO_4$  is high, the erosion wear rate of HCCI is the highest (Figure 14a, b). When the erosion angle is  $45^\circ$ , the concentration of  $H_2SO_4$  in HVCA is 6 wt% or 4 wt%. When the erosion velocity is large, the degree of erosion wear is

serious, and the erosion resistance is poor. The effect of the erosion angle on the erosion wear performance of HVCA is in the middle, second only to the concentration of sulfuric acid. Compared with the erosion angle of  $30^\circ$  and  $60^\circ$ , the HVCA has the greatest erosion wear capacity and the worst erosion resistance. When the erosion angle is  $60^\circ$ , the erosion wear amount of HVCA shows an increasing trend and reaches its maximum value when both erosion velocity and concentration are maximum. The erosion wear rate of HCCI increases with the increase in erosion wear Angle (Figure 14d, f). When the erosion wear angle is  $45^\circ$ , the

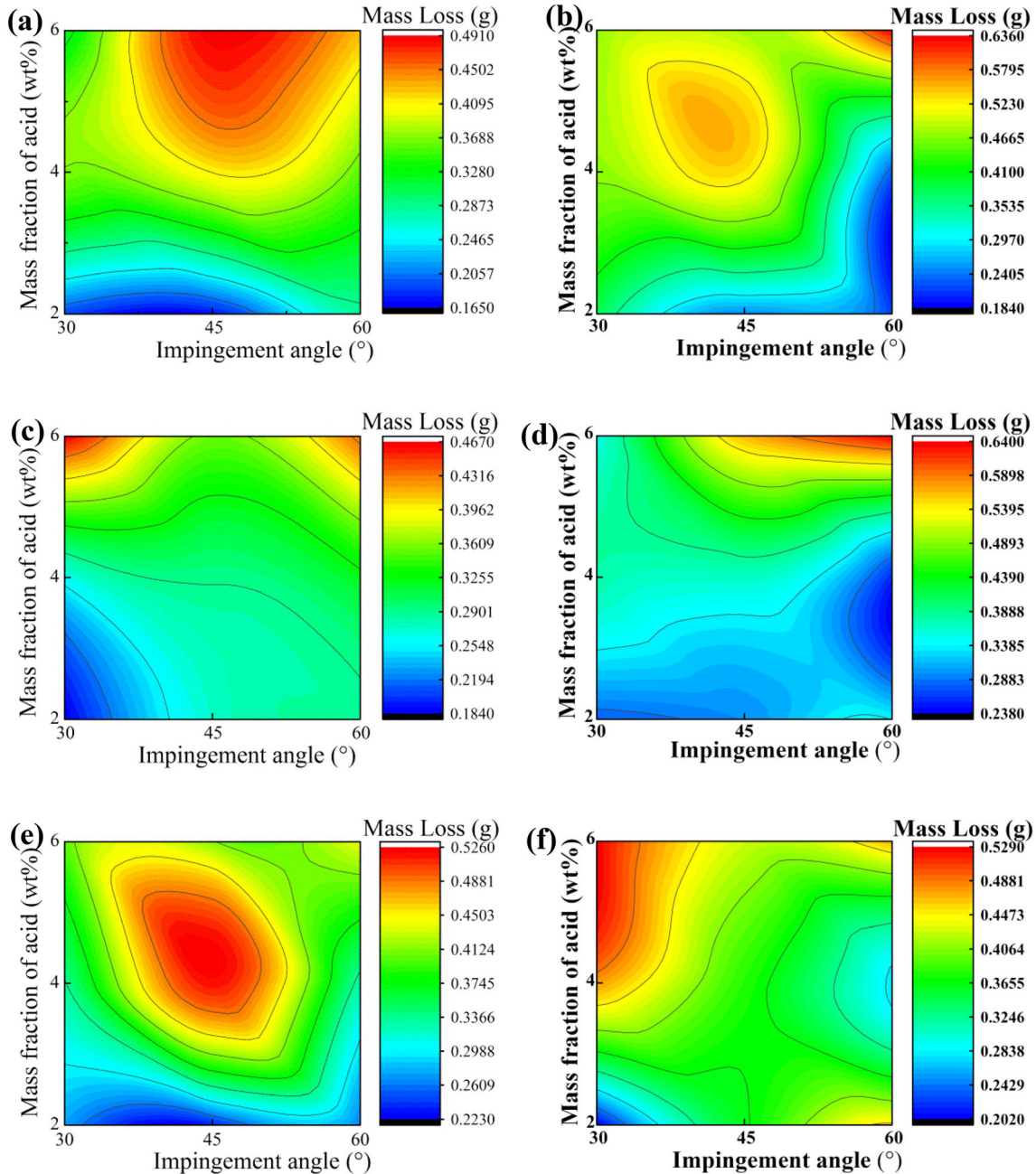


**Figure 15.** The contour plot shows the interactive effect among the influencing factors: (a) HVCA, 500 r/min; (b) HCCI, 500 r/min; (c) HVCA, 750 r/min; (d) HCCI, 750 r/min; (e) HVCA, 1000 r/min; (f) HCCI, 1000 r/min.

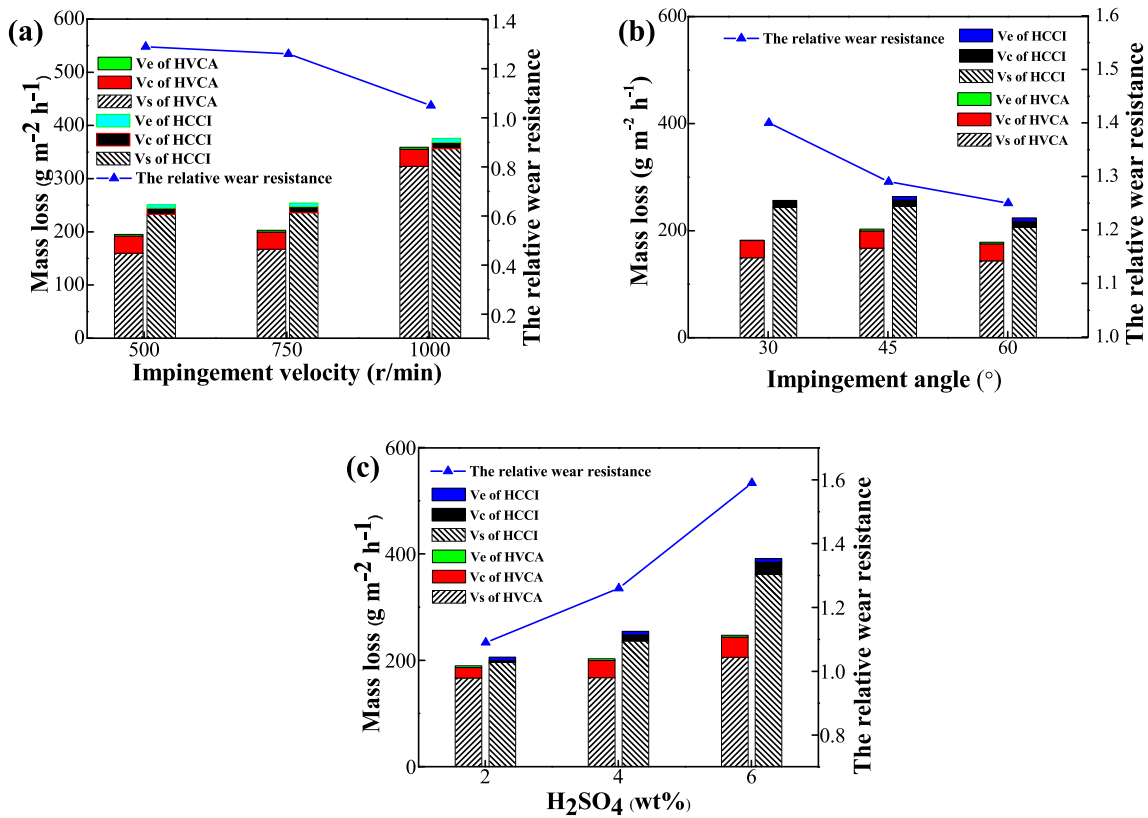


**Figure 16. The influence of erosion wear in acid sand slurry on the erosion wear rate and  $\varepsilon$  of materials: (a) impingement velocities, (b) impingement angle, (c)  $H_2SO_4$  concentration.**

HCCI erosion rate reaches the maximum at low erosion wear rate and 4 wt%  $H_2SO_4$  concentration, or at the maximum  $H_2SO_4$  concentration and medium erosion wear velocity.

Figure 15 is the contour map of the interaction between erosion wear angle and  $H_2SO_4$  concentration. With the increase in erosion wear velocity, the erosion wear of HVCA gradually increases. At low erosion wear velocity, the maximum erosion wear of HVCA occurs when the erosion wear angle is 45°. At high erosion wear velocity, when the erosion wear angle is 45° and the concentration of  $H_2SO_4$  is 4 wt%, the erosion wear of HVCA reaches the maximum. In conclusion, the erosion wear resistance of HVCA increases with the increase in erosion wear velocity and  $H_2SO_4$  concentration and decreases first and then increases with the increase in erosion angle, which is the worst at 45°. The maximum erosion wear rate of HCCI at low erosion wear velocity is basically at the maximum velocity concentration and erosion wear angle. Under high erosion wear velocity, the maximum erosion wear rate of HCCI occurs in the concentrated area of low angle and high speed.

The corrosion and wear interaction rate of materials in acid mortar  $V_s$ , pure corrosion rate  $V_c$ , pure wear rate  $V_e$  and the relative anti-erosion wear rate  $\varepsilon$  of HVCA vary with the impingement velocities, as shown in Figure 16a. It should be noted that the total height of the column chart represents the

erosion corrosion wear rate  $V_t$ , whose impingement angle is 45°, and the mass fraction of  $H_2SO_4$  is 4%. With the increase in erosion velocity, the erosion corrosion wear rate  $V_t$  of the two materials increases monotonously. It can be seen that with the increase in erosion velocity, the erosion corrosion wear resistance of the materials decreases obviously, while the HVCA with good corrosion resistance decreases less. Compared with the pure wear rate  $V_e$  in water sand slurry,  $V_t$  is dozens of times of  $V_e$ , which is greatly increased mainly due to the appearance of the interaction rate of erosion corrosion and wear  $V_s$ , which accounts for 82–90% of the total weight loss rate. The interaction rate of the two materials  $V_s$  increases significantly with the increase in impingement velocities. With the increase in erosion speed, the relative erosion wear rate ( $\varepsilon$ ) of HVCA decreases gradually. When the rotational speed of erosion wear test machine is 500 r/min,  $\varepsilon$  value reaches the maximum value of 1.29. Therefore, the erosion wear resistance of HVCA in acid sand slurry is better than that of HCCI.

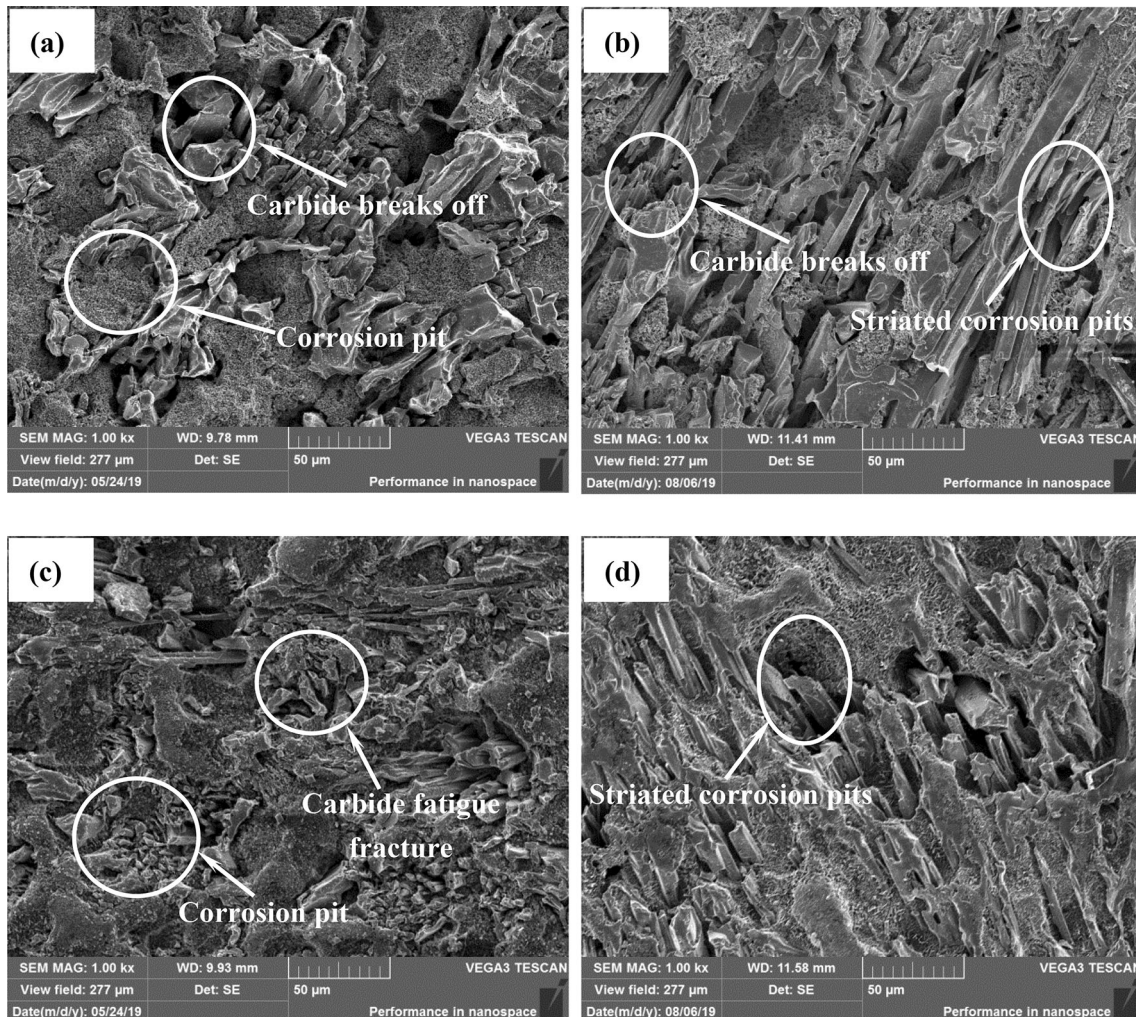
The influence of impingement angle on the erosion wear rate  $V_t$  and  $\varepsilon$  of the material is shown in Figure 16b. The impingement velocity is 750 r/min, and the mass fraction of  $H_2SO_4$  is 4%. The erosion corrosion wear rate  $V_t$  and the interaction rate of corrosion and wear  $V_s$  of HVCA are both lower than that of HCCI.  $V_t$  and  $V_s$  of both materials reach their maximum value when the impingement angle is 45°. At the same time, the relative anti-erosion wear rate of HVCA reaches the maximum value of 1.4 at 30°.

Figure 16c shows the influence of  $H_2SO_4$  concentration in acid sand slurry on the erosion wear rate of the two materials and the relative anti-erosion wear rate  $\varepsilon$  of HVCA. The impingement velocity is 750 r/min, and the impingement angle is  $45^\circ$ . With the increase in  $H_2SO_4$  concentration, the erosion wear rate of the two materials increased linearly. The relative erosion wear rate  $\varepsilon$  of HVCA increased with the increase in  $H_2SO_4$  concentration, and the maximum value of  $\varepsilon$  was 1.59. Therefore, in order to make the material have excellent erosion resistance and wear resistance, it is necessary to have excellent corrosion resistance and wear resistance at the same time, so as to reduce the interaction between corrosion and wear.

### Erosion Wear Morphology

The erosion wear morphology of materials at different impingement angles is shown in Figure 17. Acid erosion is the main erosion mechanism in acid sand slurry. The main

erosion wear mechanism in acid is acid erosion. The surface roughness of the two materials is large, and the carbide particles on the surface are prominent. Corrosion pits are the main erosion forms of HVCA. With the increase in impingement angle, the corrosion pit first increases, then deepens and then decreases. The corrosion wear is the most serious at  $45^\circ$ , accompanied by carbide fracture. The erosion wear morphology of HCCI is dominated by long strip pits. With the increase in impingement angle, the strip erosion pits on the erosion surface increase and decrease sharply. The erosion wear degree of HVCA is always lower than that of HCCI. It can be seen from the figure that corrosion is the main cause of erosion wear and its essence is phase to phase corrosion. When interphase corrosion occurs, the matrix is corroded away and a large amount of carbides are exposed. Under the action of slurry erosion, carbides are broken, and part of the matrix is peeled off. The rapid alternate shedding of the matrix and carbides results in relatively high erosion wear rate.<sup>25,26</sup> The erosion wear rate of materials in acid sand slurry is much higher



**Figure 17.** The erosion wear morphology of the material at different impingement velocities when the impingement angle is controlled at  $45^\circ$  in acid sand slurry: (a) HVCA, 500 r/min, (b) HCCI, 500 r/min (c) HVCA, 1000 r/min, (d) HCCI, 1000 r/min.

than that in water sand slurry, which is due to the interaction between corrosion and wear.<sup>27–29</sup>

When the erosion wear rate is 750 r/min, the surface wear morphology of the material under different erosion wear angles is shown in Figure 18. Under the 30° erosion wear angle, the erosion wear of the material is mainly corrosion, and the matrix is corroded, forming corrosion pits and exposing carbides. When the erosion wear angle is 45°, the

erosion wear degree of the material surface is relatively serious, which is greatly influenced by interaction between corrosion and wear. When the matrix is corroded, exposed carbides break under mechanical action. With the further increase in the erosion wear angle, the mechanical effect has a great influence on the erosion wear of the material, resulting in less carbide shedding and increased fatigue. Compared with HCCI, the erosion wear surface of HVCA is relatively flat, so it has better erosion wear performance.

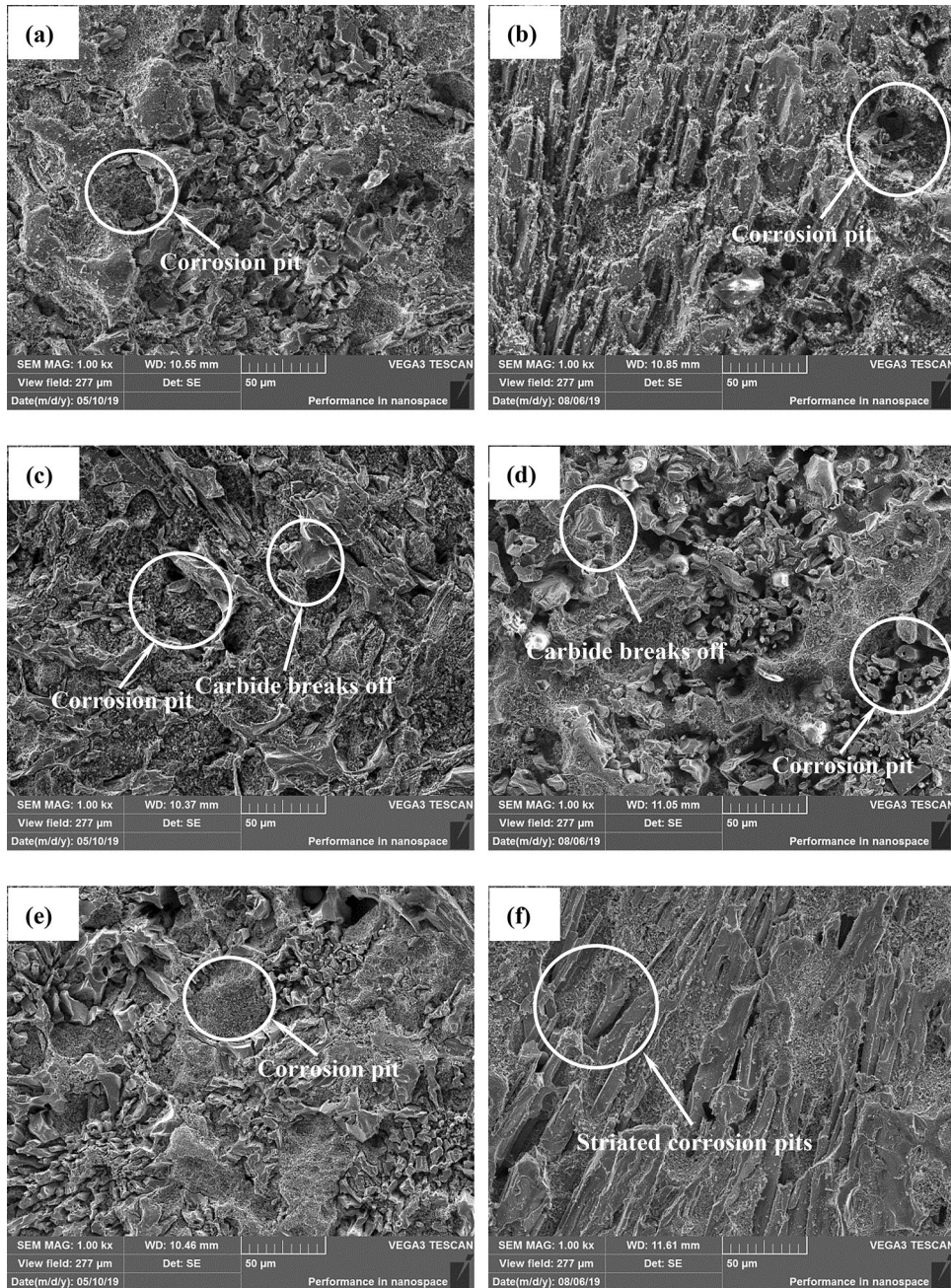


**Figure 18.** The erosion wear morphology of the material at different impingement angles when the impingement velocities is controlled at 750 r/min in acid sand slurry: (a) HVCA, 30°, (b) HCCI, 30°, (c) HVCA, 45°, (d) HCCI, 45°, (e) HVCA, 60°, (f) HCCI, 60°.

## Conclusion

1. High-vanadium–chromium alloy (HVCA) is designed and prepared by sand casting. HVCA consists mainly of austenite, martensite and carbides ( $M_7C_3$ ,  $M_{23}C_6$ , VC,  $M_2C$ ). The hardness of HVCA is 65.16 HRC, and the impact toughness reaches  $9.82 \text{ J/cm}^2$ .
2. According to orthogonal test and variance analysis,  $H_2SO_4$  concentration is the most important factor affecting erosion and wear of materials, followed by erosion wear angle.
3. The erosion wear resistance of HVCA increases with the increase in  $H_2SO_4$  concentration and decreases first and then increases with the increase in erosion angle, which is the worst at  $45^\circ$ .
4. Erosion wear is the result of the interaction of corrosion and wear. Under different test conditions, the interaction rate ( $V_s$ ) of corrosion and wear of HVCA accounted for 80.4–90% of the total erosion wear rate ( $V_t$ ). HCCI-V had better erosion wear performance than HCCI under all test conditions, and its best wear resistance was 1.59 times that of HCCI.
5. The erosion wear morphology shows that the proportion of corrosion in erosion wear is relatively large. Compared with HCCI, HVCA has shallow surface corrosion pits and less carbide fracture and peeling.
6. Compared with high-chromium cast iron, HVCA has relatively worse corrosion resistance, but its erosion wear performance is excellent. The excellent erosion wear resistance of HVCA is due to the high hardness and toughness, minor fracture and shedding of carbide and slight interaction of corrosion and wear under erosion wear condition.

## Funding

The authors greatly acknowledge the Plan for National Natural Science Foundation of China (No. 51171060) and Program for Changjiang Scholars and Innovative Research Team in University (IRT1234).

**Conflict of interest** The authors declare that they have no conflict of interest.

## REFERENCES

1. C.I. Walker, G.C. Bodkin, Empirical wear relationships for centrifugal slurry pumps: part 1: side-liners. *Wear* **242**(1–2), 140–146 (2000). [https://doi.org/10.1016/S0043-1648\(00\)00413-0](https://doi.org/10.1016/S0043-1648(00)00413-0)
2. C.I. Walker, P. Robbie, Comparison of some laboratory wear tests and field wear in slurry pumps. *Wear* **302**, 1026–1034 (2013). <https://doi.org/10.1016/j.wear.2012.11.053>
3. Y. Iwai, K. Nambu, Slurry wear properties of pump lining materials. *Wear* **210**(1–2), 211–219 (1997). [https://doi.org/10.1016/S0043-1648\(97\)00055-0](https://doi.org/10.1016/S0043-1648(97)00055-0)
4. A.A. Noon, M.H. Kim, Erosion wear on centrifugal pump casing due to slurry flow. *Wear* **364–365**, 103–111 (2016). <https://doi.org/10.1016/j.wear.2016.07.005>
5. F.G. Lu, S.Z. Wei et al., Erosion-wear behaviors of high-chromium cast iron with high nitrogen content in water-sand slurry and acid-sand slurry. *Tribol. Trans.* **63**(2), 325–335 (2019). <https://doi.org/10.1080/10402004.2019.1690082>
6. K.L. Dahm, Direct observation of the interface during sliding tribo-corrosion. *Tribol. Int.* **40**(10), 1561–1567 (2007). <https://doi.org/10.1016/j.triboint.2007.02.016>
7. H.P. Xiao, S.H. Liu et al., Abrasion-corrosion behaviors of steel-steel contact in seawater containing abrasive particles. *Tribol. Trans.* **61**(1), 12–18 (2016). <https://doi.org/10.1080/10402004.2016.1268227>
8. M. Khorasanian, M. Yeganeh et al., Effect of addition of silver and chilled casting on corrosion behavior of AZ91 magnesium alloy. *Int. J. Metalcast.* **15**, 1184–1196 (2021). <https://doi.org/10.1007/s40962-020-00558-4>
9. V. Javaheri, D. Porter et al., Slurry erosion of steel-review of tests. *Mech. Mater. Wear* **408–409**, 248–273 (2018). <https://doi.org/10.1016/j.wear.2018.05.010>
10. F.G. Lu, S.Z. Wei, L.J. Xu et al., Investigation on erosion-wear behaviors of high-chromium cast iron with high nitrogen content in salt-sand slurry. *Mater. Res. Express.* **6**(10), 106558 (2019). <https://doi.org/10.1088/2053-1591/ab39ab>
11. W.L. Song, L.J. Xu et al., Development of a new high-density iron-tungsten alloy (FWA) reinforced by  $Fe_7W_6$  and  $Fe_2W$  particles with high tensile strength and specific strength. *J. Alloys Compd.* **854**, 157323 (2021). <https://doi.org/10.1016/j.jallcom.2020.157323>
12. S.Z. Wei, L.J. Xu, Review on research progress of steel and iron wear-resistant materials. *Acta Metall. Sin.* **56**, 523–538 (2020). <https://doi.org/10.11900/0412.1961.2019.00370>
13. L.J. Xu, S.Z. Wei, M.R. Han, R. Long, Effect of carbides on wear characterization of high-alloy steels under high-stress rolling-sliding condition. *Tribol. Trans.* **57**(4), 631–636 (2014). <https://doi.org/10.1080/10402004.2014.890265>
14. X. Deng, L. Huang et al., Three-body abrasion wear resistance of TiC-reinforced low-alloy abrasion-resistant martensitic steel under dry and wet sand conditions. *Wear* **452–453**, 203310 (2020). <https://doi.org/10.1016/j.wear.2020.203310>
15. X. Chong, Y. Jiang et al., Electronic structures mechanical and thermal properties of V–C binary

- compounds. *RSC Adv.* **4**(85), 444959–444971 (2014). <https://doi.org/10.1039/c4ra07543a>
16. L.J. Xu, X.M. Fan et al., Microstructure and wear properties of high-speed steel with high molybdenum content under rolling-sliding wear. *Tribol. Int.* **116**, 39–46 (2017). <https://doi.org/10.1016/j.triboint.2017.07.002>
  17. L.J. Xu, S.Z. Wei et al., Effects of carbides on abrasive wear properties and failure behaviours of high speed steels with different alloy element content. *Wear* **376–377**, 968–974 (2017). <https://doi.org/10.1016/j.wear.2017.01.021>
  18. L.J. Xu, S.Z. Wei et al., Effects of carbon content and sliding ratio on wear behavior of high-vanadium high-speed steel (HVHSS) under high-stress rolling–sliding contact. *Tribol. Int.* **70**, 34–41 (2014). <https://doi.org/10.1016/j.triboint.2013.09.021>
  19. L.J. Xu, F.F. Wang et al., Fabrication and wear property of in-situ micro-nano dual-scale vanadium carbide ceramics strengthened wear-resistant composite layers. *Ceram. Int.* **47**(1), 953–964 (2020). <https://doi.org/10.1016/j.ceramint.2020.08.209>
  20. X.W. Qi, Z.N. Jia et al., Effects of vanadium additive on structure property and tribological performance of high chromium cast iron hardfacing metal. *Surf. Coat. Technol.* **205**(23–24), 5510–5514 (2011). <https://doi.org/10.1016/j.surfcoat.2011.06.027>
  21. Y. Uematsu, T. Kakiuchi et al., Effects of shot peening on fatigue behavior in high speed steel and cast iron with spheroidal vanadium carbides dispersed within martensitic-matrix microstructure. *Mater. Sci. Eng. A* **561**(20), 386–393 (2013). <https://doi.org/10.1016/j.msea.2012.10.045>
  22. V.G. Efremenko, G. Chabak et al., Kinetic parameters of secondary carbide precipitation in high-Cr white iron alloyed by MnNi-Mo-V complex. *J. Mater. Eng. Perform.* **22**(5), 1378–1385 (2013). <https://doi.org/10.1007/s11665-012-0434-6>
  23. Q. Liu et al., Dynamic precipitation behavior of secondary M7C3 carbides in Ti-alloyed high chromium cast iron. *ISIJ Int.* **53**(7), 1237–1244 (2013). <https://doi.org/10.2355/isijinternational.53.1237>
  24. P. Bazarnik, A. Bartkowska et al., Superior strength of tri-layered Al–Cu–Al nano-composites processed by high-pressure torsion. *J. Alloys Compd.* **846**(1–10), 156380 (2020). <https://doi.org/10.1016/j.jallcom.2020.156380>
  25. A. Siddaiah, B. Mao et al., Effect of laser shock peening on the wear-corrosion synergistic behavior of an AZ31B magnesium alloy. *J. Tribol.* **142**(4), 1–22 (2019). <https://doi.org/10.1115/1.4045500>
  26. Z.B. Zheng, S.Q. Chen et al., Effect of chromium content on the erosion-corrosion behavior of Fe–Cr alloy produced by ball milling liner in weakly alkaline slurry. *Mater. Res. Express* **7**(3), 1–22 (2020). <https://doi.org/10.1088/2053-1591/ab7b95>
  27. A. Iwabuchi, J.W. Lee et al., Synergistic effect of fretting wear and sliding wear of Co-alloy and Ti-alloy in Hanks' solution. *Wear* **263**(1), 492–500 (2007). <https://doi.org/10.1016/j.wear.2007.01.102>
  28. A.W. Batchelor, G.W. Stachowiak, Predicting synergism between corrosion and abrasive wear. *Wear* **123**, 281–291 (1988). [https://doi.org/10.1016/0043-1648\(88\)90144-5](https://doi.org/10.1016/0043-1648(88)90144-5)
  29. A. Neville, T. Hodgkiess et al., A study of the erosion-corrosion behaviour of engineering steels for marine pumping applications. *Wear* **186–187**, 497–507 (1995). [https://doi.org/10.1016/0043-1648\(95\)07145-8](https://doi.org/10.1016/0043-1648(95)07145-8)

**Publisher's Note** Springer Nature remains neutral with regard to jurisdictional claims in published maps and institutional affiliations.